ACS OMEGA

http://pubs.acs.org/journal/acsodf

Article

An Electrochemical Sensor for Sunset Yellow Detection Based on Cu@Cu_2O-BNPC Formed by Modified Porous Carbon

Feiyu Yang, Jiamin Wang, Kailiang Yin,* and Huan Pang*

Cite This: *ACS Omega* 2022, 7, 32068−32077

Read Online

ACCESS | Metrics & More | Article Recommendations | Supporting Information

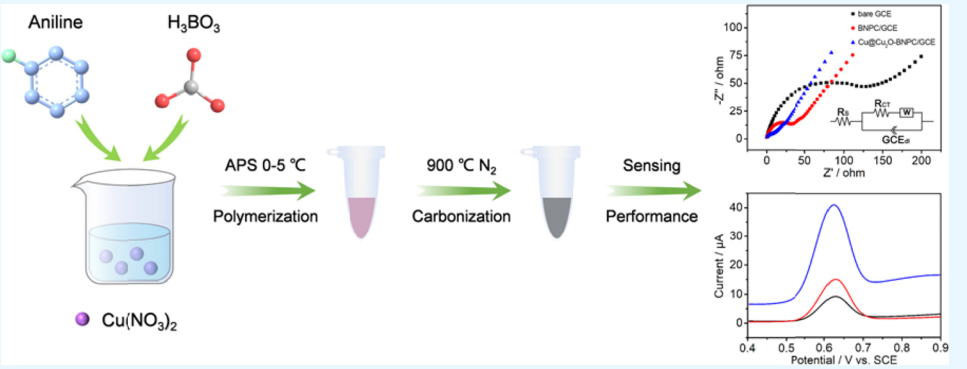

ABSTRACT: Control and detection of sunset yellow (SY) are an utmost demanding issue due to its high risk of detrimental effects on living systems caused by excessive ingestion. In this study, we reported the synthesis of Cu@Cu_2O nanoparticle-decorated B and N codoped porous carbon (BNPC) and its use in developing a novel electrochemical sensor for SY. The Cu@Cu_2O-BNPC catalyst was fabricated through single-step polymerization, followed by carbonization. Scanning electron microscopy, transmission electron microscopy, X-ray diffraction, and X-ray photoelectron spectroscopy characterization results showed that Cu@Cu_2O anchored on the porous BNPC successfully. Compared with the BNPC-modified electrode, it was found that the Cu@Cu_2O-BNPC-modified electrode showed superior electrocatalytic activity in both electrochemical impedance spectroscopy and cyclic voltammetry tests. The as-prepared Cu@Cu_2O-BNPC catalyst directly acted as a sensor for amperometric detection of SY without further assembling, which exhibited an ultrahigh sensitivity of 0.09 $\mu A\ nM^{-1}\ cm^{-2}$, a low limit of detection (2.4 nM), and a wide linear detection ranging from 10 nM to 8 μM. To further validate its possible application, the proposed method was successfully used for the determination of SY in Fanta drinks with satisfactory results.

INTRODUCTION

Porous carbon, a kind of carbon nanomaterial with diversified pore structures, is currently attracting a great amount of interest due to its exceptional performance advantages of large surface area, high electrical conductivity, excellent biocompatibility, and chemical stability.[1−3] These characteristics make porous carbon a highly trusted candidate material in sensors,[4] batteries,[5] supercapacitors,[6] eletrocatalysis,[7] and so on. Especially in the fields of electrochemical sensors and biosensors with high sensitivity, rapid detection speed, and low operating cost, porous carbon possesses great application potential.[8−10] Moreover, the unique porous structure of porous carbons has made them a good substrate for loading metal nanoparticles and/or metal oxides.[11,12] Jia et al. proposed the introduction of Ni nanoparticles into porous mesoporous carbon nanorods.[13] The characterization experiment showed that Ni nanoparticles were uniformly dispersed in the carbon nanorods successfully with enhanced surface area and pore volume. Dong et al. developed a ZnO-loaded porous carbon matrix via simple thermolysis of metal−organic frameworks (MOFs).[14] After ZnO loading, the compound material had a larger surface area and better conductivity.[14,15] Using three different Zn-based MOFs as precursors, Hussain et al. also obtained porous ZnO/C nanocomposites with more structural defects and higher conductivity.[16] Thus, the comprehensive performance has been improved greatly in the application of the electrochemical immunosensor for detecting C-reactive proteins. The above results suggest that embedding metal nanoparticles and/or metal oxides on porous carbon materials is a feasible strategy to obtain new nanocomposites with superior electrochemical performance. The distinct features such as fast electron mobility, relatively higher surface area, and

Received: May 27, 2022
Accepted: August 8, 2022
Published: August 29, 2022

unique electrochemical capability of copper (Cu) and its oxide (Cu_2O) nanoparticles have rapidly attracted our attention.[17,18] Recently, Li et al. prepared Cu_2O/Cu@porous carbon composites via anchoring Cu_2O/Cu in the porous carbon framework. Due to the doping of Cu_2O/Cu, this composite possessed abundant active reaction sites and exhibited a larger surface area of catalyst and higher catalytic activity.[19] It is worth noting that the unique structural characteristics of porous carbon can prevent the agglomeration of copper (Cu) and its oxide (Cu_2O). In addition, the composite structure formed by porous carbon and doped nanoparticles is beneficial to increase the effective contact area between the analyte and the electrode surface.[20]

Although pure carbon materials have achieved great success in electrochemical applications,[21,22] previous studies have demonstrated that chemical doping can change the spin density and charge distribution of adjacent carbon atoms and further elevate the physical and chemical activities of heteroatom-doped porous carbon materials.[23,24] Yang et al. used N, Cl codoped fluorescent carbon dots (FCDs) to detect tartrazine in beverages. Compared with pure carbon dots, N, Cl-FCDs resulted in a dramatic improvement in the fluorescence properties and surface physical chemical properties.[25] Liu et al. introduced nitrogen and phosphorus into the carbon lattice of porous carbon materials. The synergistic effect between the N atom and the P atom in the carbon matrix can significantly promote the sensor performances in conductivity and activity.[26] The above examples exhibited that heteroatoms can enhance the sensing properties of carbon by modifying carbon materials directly. Among various kinds of heteroatom-doped composites, electron-deficient B and electron-rich N-doped porous carbons have a tremendous future in electrical sensors.[27] The conjugated structure formed by the B, N bonding configuration and porous carbon can ameliorate the electrochemical properties of carbon-based compounds.[28] Furthermore, the abundant active sites on the surface of the B, N codoped carbon nanocomposites are conductive to further improving the activity of the catalysts.

In food processing, synthetic dyes are often added to color food due to their good stability in light, temperature, and pH and low price.[29,30] Sunset yellow (SY) is a typical artificial colorant that contains an azo group, which can not only achieve ideal colors but also improve the texture of foods when employed in fruit juices, cakes, sodas, cheese sauces, ice creams, canned fish, and spicy snacks.[31] Given its large number of azo (N═N) functional groups and an aromatic ring structure, the excessive intake of SY can potentially cause many adverse health effects, including allergies, eczema, migraine headaches, asthma, anxiety, and possibly cancer.[32,33] Hence, it is significant to perform quantitative studies of SY in food products.

This study reports the advantageous features of porous carbon, heteroatom, and copper (Cu) and its oxide (Cu_2O) nanoparticles and fabrication of an electrochemical sensing platform (Cu@Cu_2O-BNPC/GCE) to detect SY. Compared with the sensor only made of porous carbon-based materials, the electrochemical performance of the Cu@Cu_2O-BNPC/GCE sensor was impressively improved. In addition, accumulation time, accumulation potential, amount of Cu@Cu_2O-BNPC suspension, and pH were optimized, and the electrochemical reaction mechanism for SY was described in detail. Finally, this novel sensor was successfully applied for determining SY in actual sample of food products to ensure food safety, with cost and performance superior to that achieved using other compound materials.

EXPERIMENTAL SECTION

Chemicals and Reagents. Boric acid (H_3BO_3), aniline, ammonium persulfate (APS), and copper nitrate trihydrate ($Cu(NO_3)_2{\cdot}3H_2O$) were purchased from Shanghai Aladdin Bio-Chem Technology Co., Ltd. The aniline monomer purchased from E. Merck was purified by vacuum distillation before polymerization. SY, tartrazine, amaranth, brilliant blue G, quinoline yellow, sucrose, saccharin, glucose, vitamin C, oxalate, and sodium citrate were purchased from Sigma-Aldrich Co., Ltd. Phosphate buffer solution (PBS) was obtained via mixing different amounts of equimolar aqueous solutions of disodium hydrogen phosphate dodecahydrate (Na_2HPO_4) and sodium dihydrogen phosphate dihydrate (NaH_2PO_4), which were purchased from Sinopharm Chemical Reagent Co., Ltd. Fanta drinks were obtained from the local supermarket. All reagents were of analytical grade and could be used without further purification. High purity water (18 MΩ cm) was used to prepare all aqueous solutions throughout our study.

Apparatus. Electrochemical experiments were conducted at 25 ± 1 °C using an electrochemical workstation (CHI660E) and a conventional three-electrode system, which consists of a glassy carbon working electrode (GCE, diameter: 3 mm), a platinum column counter electrode, and a saturated calomel reference electrode (SCE). The techniques of differential pulse voltammetry (DPV) and cyclic voltammetry (CV) were used to explore the SY detection performance of the as-prepared modified electrode. pH values were measured using a clean pH meter (PHS-3C) with the combined pH glass electrode.

The surface morphology and structure of the as-prepared samples were observed using the Zeiss Supra field-emission scanning electron microscope (FESEM) and the Tecnai G2 F30 S-Twin high-resolution electron microscope (HRTEM). Powder X-ray diffraction (XRD) patterns were collected using a Bruker D8 Advance X-ray diffractometer, which is equipped with Cu Kα radiation (λ = 0.154 nm). Raman spectra were collected using a Renishaw inVia microscope. X-ray photoelectron spectroscopy (XPS) analysis was conducted using an Axis Ultra X-ray photoelectron spectroscope equipped with Al Kα radiation of 1486.6 eV.

Preparation of Cu@Cu_2O-BNPC. A common synthesis method of Cu@Cu_2O-BNPC is as follow: First, two ice cold equimolar solutions of aniline (50 mM) and APS (50 mM) were separately dissolved into 1 M H_3BO_3 followed by rapid mixing and 30 min of stirring treatment at ice cold temperature. After this, the solution of $Cu(NO_3)_2$ (50 mM) was added to the above mixed solution drop by drop and stirred continuously at 0∼5 °C for 12 h under an N_2 atmosphere. Second, the reaction solution was centrifuged and repeatedly washed with deionized water until a pH value of 7 was reached. After drying at 60 °C under vacuum, the acquired solids were heated at 900 °C with a heating rate of 5 °C min^{-1} under an N_2 atmosphere and maintained at this temperature for 2 h to generate the final Cu@Cu_2O-BNPC powder. On the other hand, BNPC, which served as a counterpart sample for comparison purpose, was also prepared in the same manner excluding the addition of the $Cu(NO_3)_2$ solution.

Preparation of the Cu@Cu_2O-BNPC-Modified Electrode. The GCE was first polished with 0.3 μm Al_2O_3 slurry and cleaned thoroughly with water and ethanol followed by

https://doi.org/10.1021/acsomega.2c03319
ACS Omega 2022, 7, 32068−32077

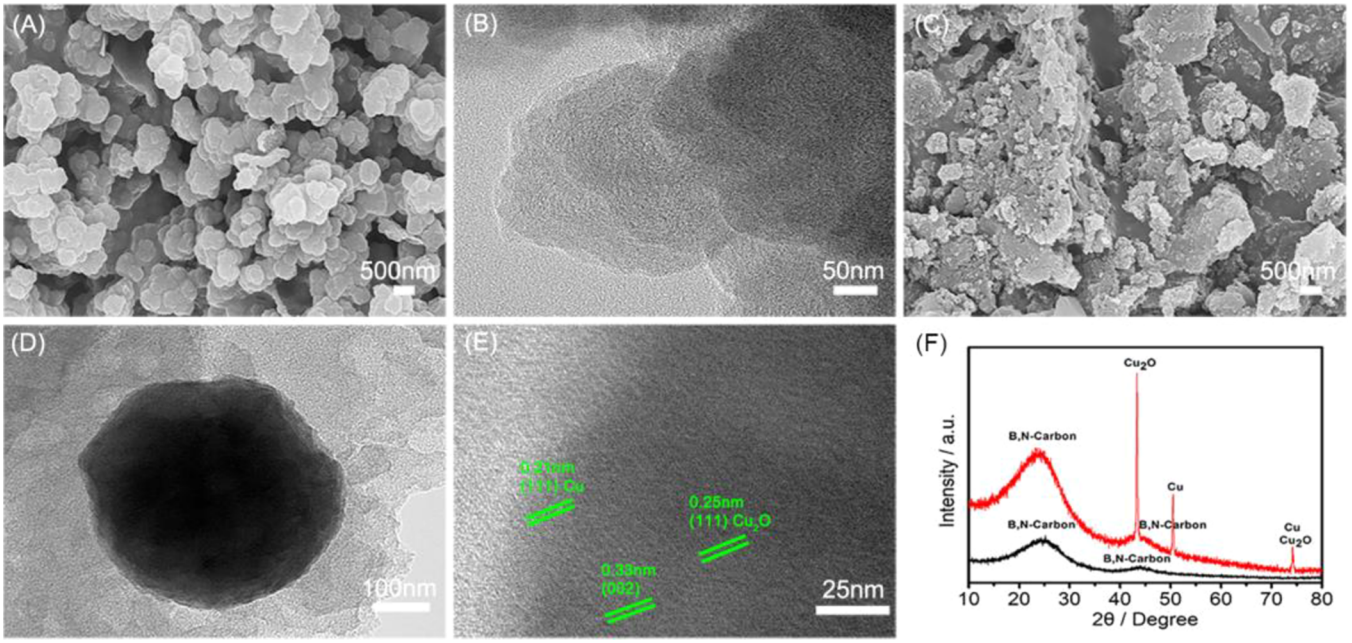

Figure 1. SEM (A) and TEM (B) images of BNPC; SEM (C), TEM (D), and HRTEM (E) image of Cu@Cu_2O-BNPC; and XRD patterns (F) of BNPC (black line) and Cu@Cu_2O-BNPC (red line).

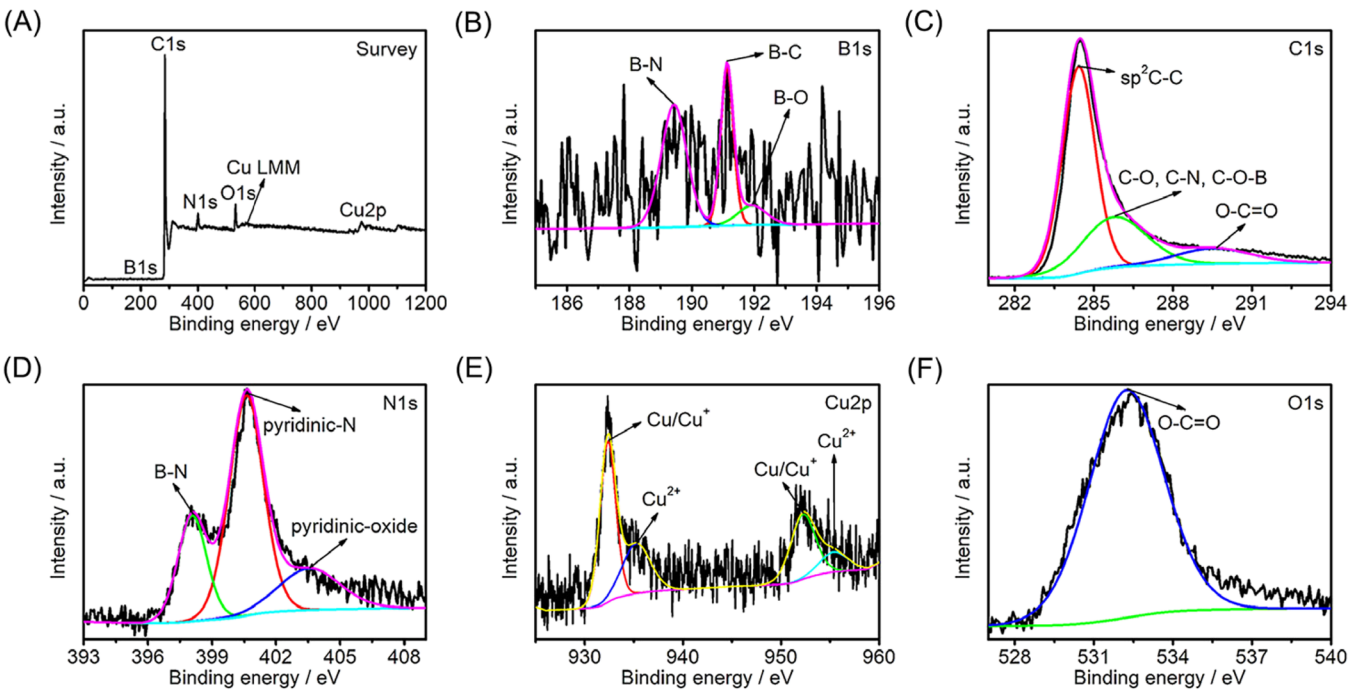

Figure 2. High-resolution XPS spectra for (A) survey, (B) B 1s, (C) C 1s, (D) N 1s, (E) Cu 2p, and (F) O 1s of Cu@Cu_2O-BNPC.

drying under an N_2 atmosphere. Afterward, 2.0 mg of Cu@Cu_2O-BNPC sample was dispersed in 1.0 mL of deionized water. Finally, 5.0 μL of the above dispersion was added onto the prefabricated GCE surface and air-dried naturally. When not in use, the modified electrodes were stored at 4 °C in a refrigerator.

RESULTS AND DISCUSSION

Surface Characterization of Cu@Cu_2O-BNPC. The surface morphology, dimension, and structure of the prepared Cu@Cu_2O-BNPC were analyzed using scanning electron microscopy (SEM) and transmission electron microscopy (TEM). Figure 1A shows the SEM image of BNPC as foam-like carbon sheets. After incorporation of Cu@Cu_2O, numerous nanospheres were uniformly embedded in the carbon sheets (Figure 1C). The typical low-magnification TEM image displayed a thin sheet-like structured BNPC carbon matrix (Figure 1B). Figure 1D shows the changes during incorporation of Cu@Cu_2O into BNPC, which plainly exhibits that sphere-like Cu@Cu_2O nanoparticles with a mean size around 200 nm were homogeneously distributed throughout the thin carbon sheets without any agglomeration.

https://doi.org/10.1021/acsomega.2c03319
ACS Omega 2022, 7, 32068−32077

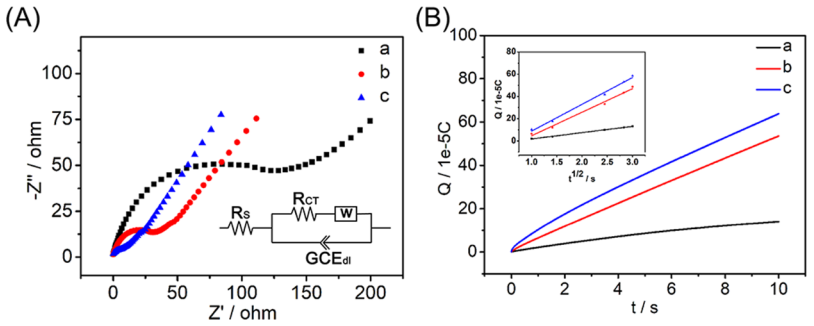

Figure 3. (A) Nyquist plots and (B) saturated adsorption capacity of bare GCE (a), BNPC/GCE (b), and Cu@Cu_2O-BNPC/GCE (c).

By comparison, the amorphous carbon presented a distinctive sheet-like structure with a porous surface. The detailed crystallographic structure of the composite was studied by HRTEM. In Figure 1E, the calculated "*d*" spacing values of the lattice fringes of the nanoparticles were 0.21 and 0.25 nm, which correspond to the (111) planes of both Cu and Cu_2O, implying the presence of the above two components.[34] An additional HRTEM image of the resulting composite showed that the graphitic carbon enwrapped a large amount of nanoparticles with a 0.33 nm *d* spacing, indicating that the nanoparticles and graphitic carbon have a close interfacial connection. The enhanced electrocatalytic properties of the nanocomposites are ascribed to the innermost connection between Cu@Cu_2O and BNPC.

The purity and structure of the Cu@Cu_2O-BNPC catalyst have been measured by XRD.[35] In the XRD patterns shown in Figure 1F, two broad diffraction peaks of BNPC (black line) at around 25° and 43° correspond to the (002) and (101) reflections of a graphite phase, which certified the formation of BNPC. Remarkably, the similar diffraction pattern of Cu@Cu_2O-BNPC (red line) portraying peaks at around 25° and 43° indicated the formation of graphitic carbon. The rest of the sharp peaks could be precisely indexed with the face centered cubic form of Cu (JCPDS 04-0836) and Cu_2O (JCPDS 05-0667).[36,37] Significantly, no formation of diffraction peaks of other possible elemental impurities has confirmed the high-phase crystallographic purity of Cu@Cu_2O-BNPC.

In sequence to the morphological analysis, the resulting Cu@Cu_2O-BNPC composite was characterized using XPS tests to determine the elemental composition and oxidation states of the surface. As shown in Figure 2A, the full XPS survey spectrum of Cu@Cu_2O-BNPC indicated the presence of coexisting B, C, N, Cu, and O elements in the composite. After Gaussian fitting, the enlarged B 1s signal was composed of three peaks situated at around 189.8, 191.3, and 192 eV, corresponding to B−N, B−C, and B−O, respectively (Figure 2B). Moreover, the high-resolution C 1s spectrum shown in Figure 2C was deconvoluted into three peaks corresponding to the sp^2-hybridized graphite-like carbon (C−C sp^2) bonding at 284.9 eV, C−O/C−N/C−O−B bonding at 285.8 eV, and O−C═O bonding at 289.2 eV.[38] In addition, the N 1s high-resolution spectrum could be deconvoluted into triplet peaks at 398.1, 400.3, and 403.1 eV, which were the characteristic peaks of B−N, pyridinic-N, and pyridinic oxide (Figure 2D).[28,39,40] The presence of pyridinic-N can result in an improved electrochemical reaction rate and electrical conductivity of Cu@Cu_2O-BNPC.[41] In addition, the Cu 2p spectrum shown in Figure 2E was fitted into a dual peak located at 934.5 and 954.0 eV, corresponding to the Cu $2p_{3/2}$ and Cu $2p_{1/2}$ binding energies, respectively. The spin orbital of Cu $2p_{3/2}$ can be further deconvoluted into two peaks at 933.5 and 936.1 eV, indicating the presence of Cu/Cu^+ and Cu^{2+}. Considering that the binding energy of Cu is close to that of Cu_2O (Figure 2E), we could distinguish them via the position of their LMM Auger transition at 568 eV (Cu^0) and 571 eV (Cu^{1+}),[42,43] denoting the existence of both the above substances. These results were in agreement with the XRD analysis of the resulting samples. For the O 1s spectrum, the peak at 532.6 eV displayed in Figure 2F could be related to O−C═O, which was consistent with that of C 1s spectrum.[44] In conclusion, the abundant surface chemical composition may offer an elevated catalytic activity to Cu@Cu_2O-BNPC.

Electrochemical Properties of Cu@Cu_2O-BNPC. Electrochemical impedance spectroscopy (EIS) renders valuable information about the electrode surface when comparing the results obtained with the bare and the modified electrode surfaces. Figure 3A shows the obtained Nyquist plots of the three target electrodes (bare GCE, BNPC/GCE, and Cu@Cu_2O-BNPC/GCE) in a mixed solution with 5.0 mM Fe(CN)3−/4−6:0.1 M KCl = 1:1. The large well-shaped semicircle of the bare GCE indicates the transfer of electrons on the GCE interface. However, BNPC/GCE (b) and Cu@Cu_2O-BNPC/GCE (c) exhibited semicircles with a significantly decreased diameter at the high-frequency region. According to the inset graph of Randles equivalent circuits, the electron transfer resistance (R_{ct}) values were calculated to be 112.41, 26.30, and 12.62 Ω on the bare GCE (a), BNPC/GCE (b), and Cu@Cu_2O-BNPC/GCE (c), respectively. The R_{ct} value of the electrode modified with BNPC is greatly reduced, indicating that it has stronger charge-transfer ability, which is mainly attributed to the excellent conductivity of graphene. When the Cu@Cu_2O-BNPC film is coated on the surface of bare GCE (a), the charge-transfer ability is further augmented and the R_{ct} value reached a minimum, which is due to the high surface area of the nanocomposite. Clearly, Cu@Cu_2O-BNPC possesses the largest ionic conductivity according to the results of EIS measurements.

It is worth noting that the ionic conductivity is related to the degree of graphitization.[45] The Raman spectrum can be used to explain the change in the degree of graphitization. As shown in Figure S1, both samples displayed two dominant broad peaks at around 1350 and 1586 cm^{-1}, which were associated with the disorders and defects (D-band) in the graphite sheets and the sp^2 feature (G-band) in the graphitic carbon, respectively. The ratio of D-band to G-band (I_D/I_G) is usually used to semiquantitatively evaluate the level of graphitic nature of carbon materials.[46] In this study, compared with BNPC, a higher I_D/I_G band intensity ratio value was obtained for Cu@

https://doi.org/10.1021/acsomega.2c03319
ACS Omega 2022, 7, 32068−32077

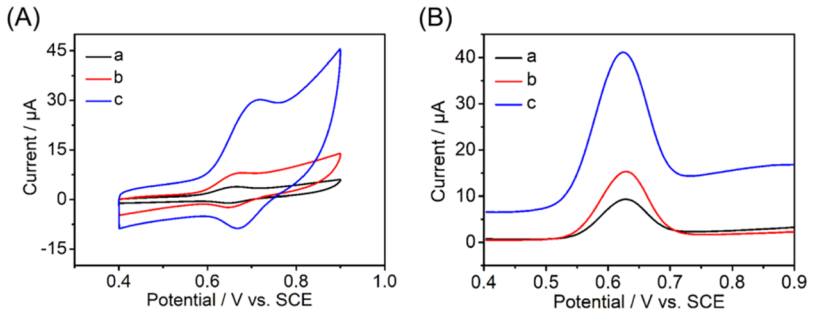

Figure 4. (A) CV curves and (B) DPV curves of SY at bare GCE (a), BNPC/GCE (b), and Cu@Cu_2O-BNPC/GCE (c).

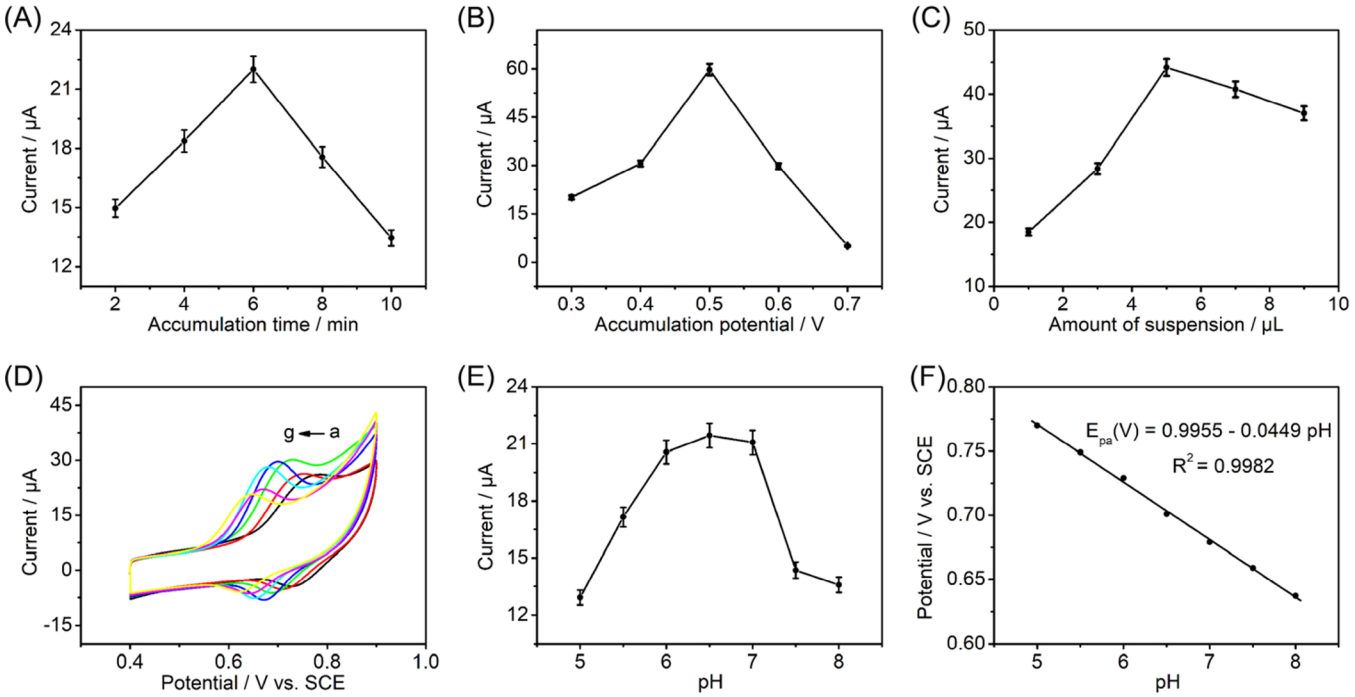

Figure 5. Effects of accumulation time (A), accumulation potential (B), and amount of Cu@Cu_2O-BNPC suspensions (C) on the oxidation peak currents of 5 μM SY (error bar represents the standard deviation of triple measurements). (D) CV curves of 5 μM SY in a supporting electrolyte solution with different pH values (a–g: 5.0–8.0). (E) Effects of pH value on the oxidation peak currents of SY. (F) Linear calibration curve of E_{pa} versus pH.

Cu_2O-BNPC, which implied that Cu@Cu_2O doping generated more defect sites than pure BNPC. Herein, the Raman spectrum results verified the reasons for increased ionic conductivity of Cu@Cu_2O-BNPC.

To further evaluate the active areas of the resulting electrodes, chronocoulometry was conducted (Figure 3B). The saturated adsorption capacities of bare GCE, BNPC/GCE, and Cu@Cu_2O-BNPC/GCE are calculated in the mixed solution with $K_3Fe(CN)3-/4-6$ (1 mmol L^{-1}) and KCl (0.1 mol L^{-1}). The linear relationship between the electric quantity (Q) and $t^{1/2}$ is expressed as the equations: Q(GCE) = $5.6406t^{1/2} - 3.8726$ (R^2 = 0.9958), Q(BNPC/GCE) = $22.1057t^{1/2} - 19.5382$ (R^2 = 0.9902), and Q(Cu@Cu_2O-BNPC/GCE) = $24.8908t^{1/2} - 17.9479$ (R^2 = 0.9941). Hence, the active areas of different electrodes could be calculated according to the formula:

$$Q = \frac{2nFAcD^{1/2}t^{1/2}}{\pi^{1/2}} + Q_{dl} + Q_{ads}$$

where Q_{dl} and Q_{ads} represent the double-layer charge and Faraday charge, respectively, A is the effective area of the modified electrode, c is the concentration of the substrate, and F is the Faraday constant (96,485 C mol^{-1}). In particular, for the $K_3Fe(CN)_6$ solution, the number of electrons transferred (n) is 1 and the diffusion coefficient (D) is 7.6×10^{-6} cm^2 s^{-1}. The active areas of the three working electrodes are, respectively, calculated to be 18.79, 73.65, and 82.93 mm^2 using the slope of the regression equation of $Q \sim t^{1/2}$. It is worth noting that Cu@Cu_2O-BNPC/GCE possessed the largest active area, which can be ascribed to the composite structure formed by BNPC and Cu@Cu_2O nanospheres. In other words, Cu@Cu_2O-BNPC shows a higher electron conduction rate, which is consistent with the EIS results.

Electrochemical Sensing of SY. In order to clarify the electrochemical performance and explore the optimum detection activity toward SY, a range of CV tests of the Cu@Cu_2O-BNPC sample are conducted. Figure 4A reveals the electrochemical oxidation activity in the presence of 5 μM SY at the bare GCE (curve a), BNPC/GCE (curve b), and Cu@Cu_2O-BNPC/GCE (curve c). When adding SY, each of the

https://doi.org/10.1021/acsomega.2c03319
ACS Omega 2022, 7, 32068–32077

Scheme 1. Mechanism for the Electrochemical Oxidation of SY

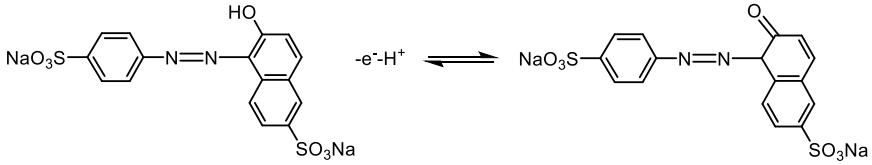

three curves exhibited a couple of obvious redox peaks, demonstrating that SY can be reversibly oxidized on the surface of all the electrode materials. From the curves c to a, the calculated oxidation signal values of 5 μM SY are about 30.80, 7.56, and 3.28 μA, respectively. Compared with the bare electrode, the BNPC electrode exhibited a higher oxidation signal, which is mainly attributed to the excellent conductivity and catalytic activity provided by the modified substance. When Cu@Cu_2O-BNPC was immobilized on the GCE surface, the significantly increased value of the oxidation peak signal demonstrates that the above nanocomposite is conducive to promoting electron transfer and improving electrode conductivity.

Compared to CV tests, DPV can provide more obvious peak shape and higher sensitivity.[47] Figure 4B exhibits the DPV responses of the three as-prepared GCE in pH = 6.5 phosphate buffer containing 5 μM SY; the order of the SY oxidation response current is Cu@Cu_2O-BNPC/GCE (curve c) > BNPC/GCE (curve b) > bare GCE (curve a). Compared to the weak oxidation signal of the bare GCE at 0.63 V, Cu@Cu_2O-BNPC/GCE and BNPC/GCE possessed significantly enhanced response signals of SY, especially the Cu@Cu_2O-BNPC composite, indicating that SY exhibited better oxidation activity on the surface of the modified electrodes. All the above results can be ascribed to the synergetic effect between BNPC and Cu@Cu_2O nanospheres and the unique physiochemical properties of the Cu@Cu_2O-BNPC composite including high surface area, rapid ion diffusion rate, and abundant active sites.

Optimization of the Experimental Parameters. In order to obtain the best sensing property, the electrochemical sensor performance of the Cu@Cu_2O-BNPC electrode was further explored with respect to the influences of accumulation time, accumulation potential, amount of suspension, and pH value.

Effect of Accumulation Time. By increasing the accumulation time, the amount of SY loaded on the electrode surface is gradually increased, accompanied by the enhancement of the oxidation signal for SY. Figure 5A displays the peak current value of Cu@Cu_2O-BNPC at different accumulation times. It could be clearly seen that in the low accumulation time range (2, 4, and 6 min), the peak current reached the highest value at 6 min, which is ascribed to the abundant amount of SY on Cu@Cu_2O-BNPC/GCE. However, further increasing the accumulation time from 6 to 10 min resulted in a significant reduction of current, indicating that SY reached the load limit on the surface of the Cu@Cu_2O-BNPC film. Therefore, 6 min is selected as the optimal accumulation time.

Effect of Accumulation Potential. The effect of accumulation potential on the oxidation signal of the analyte was determined. Figure 5B presents that with the increase of accumulation potential from 0.10 to 0.70 V, the signal increased first and then decreased and reached the maximum at 0.50 V. This result indicates that 0.50 V can be used as the optimum initial potential and accumulation potential to promote the Cu@Cu_2O-BNPC electrode to exhibit the strongest response signal.

Effect of the Amount of Cu@Cu_2O-BNPC Suspension. Figure 5C depicts the effect of the modification amount of Cu@Cu_2O-BNPC suspension on the oxidation signal of SY. The response current increased gradually as the amount of the Cu@Cu_2O-BNPC suspension increased from 1 to 5 μL. However, the oxidation signal decreased on further increase of the amount of the Cu@Cu_2O-BNPC suspension to 9 μL. The above results are attributed to the increase of the film thickness of the Cu@Cu_2O-BNPC suspension, further causing a significant increase of R_{ct}. For achieving higher sensitivity, the optimal amount of the Cu@Cu_2O-BNPC suspension was adopted at 5 μL.

Effect of pH Value. Moreover, pH value is also a major parameter affecting the response signal of SY on the electrode surface. Different pH values will influence the peak value and peak position of the response signal. According to the linear fitting relationship between the pH value and the corresponding potential, the number of transferred electrons and protons in the electrochemical reaction can be obtained, and the redox mechanism of SY occurring on the electrode surface can be inferred. We explored the electrochemical response of the analyte at different pH values (5.0−8.0) using CV tests (Figure 5D). Figure 5E shows that the peak current first increased and then gradually declined with the increase of the pH value of PBS, and the Cu@Cu_2O-BNPC electrode exhibited the largest current response at pH = 6.5. Considering the higher signal strength, the supporting electrolyte is determined as PBS with pH = 6.5. In Figure 5F, as the pH was gradually increased, the oxidation peak potential (E_{pa}) shifted toward negative with the linearization equation of E_{pa} (V) = 0.9955 − 0.0449 pH (R^2 = 0.9982). The absolute value of the slope was 44.9 mV pH^{-1}, suggesting that one proton and one electron transferred between the electrode and the supporting electrolyte.[48] As displayed in Scheme 1, we inferred the redox mechanism of SY. In addition, the reduction of the electrode reaction rate caused by the load on the electrode surface leads to the deviation of this slope from the theoretical value.[49−51]

Study of Scan Rate. Next, the electrochemical behavior of SY was assessed at different scan rates using CV tests. As shown in Figure S2, the anodic and cathodic peak currents of SY increase linearly with the scan rate from 100 to 700 mV s^{-1} (a∼j). The anode spikes keep moving in the positive direction while the cathode spikes keep moving in the negative direction, suggesting that the oxidation of SY on our sensor is a reversible process. In addition, with the increase of the scan rate, the plot of I_p versus $\nu^{1/2}$ also shows linear behaviors in the inset for SY. The regression equations are I_{pa} (μA) = 1.6669$\nu^{1/2}$ − 6.3926 (R^2 = 0.9997) and I_{pc} (μA) = −0.7538$\nu^{1/2}$ + 6.9853 (R^2 = 0.9991), respectively. The result indicates that the electro-oxidation process of the modified electrode surface is mainly controlled by diffusion, which is coherent well with the classical Cu-based sensor reported in the literature.[38,52]

https://doi.org/10.1021/acsomega.2c03319
ACS Omega 2022, 7, 32068−32077

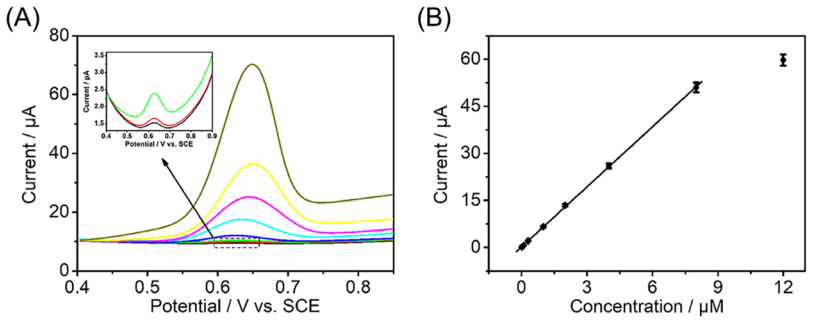

Figure 6. (A) DPV curves of Cu@Cu_2O-BNPC/GCE fabricated with different SY concentrations. (B) Corresponding linear calibration curve of panel (A) (n = 5 for each point).

Determination of SY Using Cu@Cu_2O-BNPC/GCE. We explored the variation trend of DPV peak currents for Cu@Cu_2O-BNPC/GCE with the increase of the SY concentration. As shown in Figure 6A, the current response displayed a great linear relationship with the concentration of SY ranging from 10 nM to 8 μM under the optimal test conditions. The corresponding regression equation of Cu@Cu_2O-BNPC/GCE is I_{pa} (μA) = 6.3834C (μM) + 0.1971 (R^2 = 0.9997) (Figure 6B). In addition, the calculated limit of detection (LOD) was about 2.4 nM when S/N = 3. The sensitivity of the Cu@Cu_2O-BNPC-based sensor was also calculated to be 0.09 μA nM^{-1} cm^{-2}. With the analyte concentration exceeding 8 μM, the deviation of the calibration plot indicated that the surface of the modified electrode had been in a saturated state. Overall, the constructed Cu@Cu_2O-BNPC sensor offered a relatively wider linear range, lower LOD, and ultrahigh sensitivity for SY detection.

Comparison of the Sensor Performance. As shown in Table 1, the resulting modified electrode has a considerable advantage in terms of LOD and linear interval than other electrode samples reported in the previous literature. This comparison proved that the electrochemical sensing platform constructed using Cu@Cu_2O-BNPC as a modified material is suitable for SY detection.

Table 1. Comparison of the Detection Performance of Reported SY Sensors

electrode materials	linear range (μM)	LOD (nM)	refs
MWCNT-GCE	0.55~7	120	42
GN/TiO_2-CPE	0.02~2.05	6	43
ZnO/RGO/ZnO@Zn/GCE	0.05~5	3	53
ERGO-AuNRs-GCE	0.01~3	2.4	54
GO-MWCNTs-GCE	0.09~8	25	55
Pt/GCE	0.0316~3.16	31.6	56
nAu/CPE	0.1~2	30	57
Cu_2O-ErGO/GCE	0.02~20	6	58
Cu@Cu_2O-BNPC/GCE	0.01~8	2.4	this work

Selectivity, Repeatability, Reproducibility, and Stability of Cu@Cu_2O-BNPC/GCE. A selectivity test was performed in order to evaluate the anti-interference ability of a Cu@Cu_2O-BNPC-modified sensor. As shown in Figure S3, the pure SY solution and the mixed solution of SY and other analogues (e.g., molecules with similar structures and possible coexisting additives) had produced almost the same amperometric responses for Cu@Cu_2O-BNPC/GCE, indicating the high selectivity of the as-proposed sensor. Next, after five consecutive tests under the same experimental conditions, SY produced nearly constant peak current and potential for the as-prepared electrode (Figure S4A). The above experimental results illustrate the good repeatability of the Cu@Cu_2O-BNPC composite. In addition, the reliability of a sensor is another crucial evaluation parameter. Here, reproducibility was investigated by analyzing the current response of five Cu@Cu_2O-BNPC electrode-prepared sensors by testing the same concentration of SY. As shown in Figure S4B, the peak current and potential of SY were similar.

Stability, a reliable index in electrochemical sensor applications, can be quantitatively defined via testing the same modified electrode once a week. Notably, after 30 days, the retention of the current response is 98.56%, suggesting that the resulting Cu@Cu_2O-BNPC film was not contaminated and had excellent long-time stability.

Practical Application of Cu@Cu_2O-BNPC/GCE. Finally, in order to explore the practical utility of the resulting composite, the Cu@Cu_2O-BNPC/GCE sensor was applied to detect SY levels in Fanta drinks. Considering the influence of the matrix on the experimental results, we adopted the standard addition method to measure the content of SY in Fanta drinks, as listed in Table 2. The obtained sample was tested independently for three times, and the recoveries of 96–103% indicated the excellent precision and real-world reliability. In addition, the relative standard deviation (RSD) ranging from 1.10 to 3.52% proved the good experimental stability of the sensing platform. In summary, Cu@Cu_2O-BNPC/GCE is a suitable electrochemical sensing platform for real beverage sample detection.

Table 2. Spiked Recovery Results for SY in a Real Sample (n = 3)

sample Fanta	added (μM)	predicted (μM)	detected (μM)	recovery (%)	RSD (%)
1	0		0.72		
2	1	1.72	1.68	96	1.10
3	2	2.72	2.78	103	2.33
4	5	5.72	5.60	97.6	3.52

CONCLUSIONS

In summary, we reported the synthesis of a Cu@Cu_2O nanoparticle-decorated BNPC and its use in developing a novel electrochemical sensor for SY. The Cu@Cu_2O-BNPC catalyst was systematically studied through a series of detailed structural characterizations and in-depth electrochemical analyses. The result shows that Cu@Cu_2O was successfully

https://doi.org/10.1021/acsomega.2c03319
ACS Omega 2022, 7, 32068−32077

anchored on the porous BNPC. Owing to the synergistic catalysis of copper-based materials and BNPC, the electron transfer ability and accumulation efficiency were improved significantly. Under optimized conditions, the Cu@Cu_2O-BNPC-based sensing platform exhibited excellent electrochemical activities toward the detection of SY with sensing bounds from 10 nM to 8 μM. The fabricated sensor was employed for the determination of SY in Fanta drinks with satisfactory results.

■ ASSOCIATED CONTENT

Supporting Information

The Supporting Information is available free of charge at https://pubs.acs.org/doi/10.1021/acsomega.2c03319.

Typical Raman spectra of BNPC and Cu@Cu_2O-BNPC, CV curves of 5 μM SY at different scan rates, influence of interferents on the detection ability of SY, and repeatability and reproducibility of Cu@Cu_2O-BNPC/GCE for the determination of SY (PDF)

■ AUTHOR INFORMATION

Corresponding Authors

Kailiang Yin − *School of Petrochemical Engineering, Changzhou University, Changzhou, Jiangsu 213164, P.R. China*; Email: klyin@cczu.edu.cn, kailiangyin@126.com

Huan Pang − *School of Chemistry and Chemical Engineering, Yangzhou University, Yangzhou, Jiangsu 225002, P.R. China*; orcid.org/0000-0002-5319-0480; Email: huanpangchem@hotmail.com, panghuan@yzu.edu.cn

Authors

Feiyu Yang − *School of Petrochemical Engineering, Changzhou University, Changzhou, Jiangsu 213164, P.R. China*

Jiamin Wang − *School of Food Science and Technology, Yangzhou University, Yangzhou, Jiangsu 225127, P.R. China*

Complete contact information is available at: https://pubs.acs.org/10.1021/acsomega.2c03319

Author Contributions

K.Y. designed this study and supervised the experimental work; F.Y. performed the synthesis, characterizations, and experiments; J.W. contributed to the data analysis; and F.Y. wrote the paper with support from K.Y. and H.P.. All authors contributed to the general discussion.

Notes

The authors declare no competing financial interest.

■ ACKNOWLEDGMENTS

Funding for this work was provided by the National Natural Science Foundation of China (32001743) and the Natural Science Fund for Colleges and Universities in Jiangsu Province (BK20180922). In addition, we thank the Testing Center of Yangzhou University for all the characterizations.

■ REFERENCES

(1) Zhang, Y.; Zhang, L.; Cheng, L.; Yang, D. D.; Wan, L.; Du, C.; Chen, J.; Xie, M. J. Synthesis of faradaic-active N,O-doped carbon nanosheets from m-trihydroxybenzene and piperazine for high-performance supercapacitor. *Appl. Surf. Sci.* **2021**, *538*, 8.

(2) ben Mosbah, M.; Mechi, L.; Khiari, R.; Moussaoui, Y. Current State of Porous Carbon for Wastewater Treatment. *Processes* **2020**, *8*, 1651.

(3) Niu, J.; Liang, J. J.; Shao, R.; Liu, M. Y.; Dou, M. L.; Li, Z. L.; Huang, Y. Q.; Wang, F. Tremella-like N,O-codoped hierarchically porous carbon nanosheets as high-performance anode materials for high energy and ultrafast Na-ion capacitors. *Nano Energy* **2017**, *41*, 285−292.

(4) Li, F.; Liu, R. Q.; Dubovyk, V.; Ran, Q. W.; Li, B.; Chang, Y. Q.; Wang, H. L.; Zhao, H. Y.; Komarneni, S. Three-dimensional hierarchical porous carbon coupled with chitosan based electrochemical sensor for sensitive determination of niclosamide. *Food Chem.* **2022**, *366*, No. 130563.

(5) Zhu, S. Q.; Huang, A. M.; Wang, Q.; Xu, Y. MOF-derived porous carbon nanofibers wrapping Sn nanoparticles as flexible anodes for lithium/sodium ion batteries. *Nanotechnology* **2021**, *32*, 10.

(6) Zhang, W.; Lin, M. H.; Cheng, R. R.; Li, L. L.; Sun, Y. X.; Ran, S. L.; Lv, Y. H.; Ma, L. B. Molten metal chloride salt template synthesis of N/S co-doped porous carbon nanosheets for supercapacitors. *Diamond Relat. Mater.* **2021**, *113*, 9.

(7) Nadeem, M.; Yasin, G.; Arif, M.; Tabassum, H.; Bhatti, M. H.; Mehmood, M.; Yunus, U.; Iqbal, R.; Nguyen, T. A.; Slimani, Y.; Song, H. H.; Zhao, W. Highly active sites of Pt/Er dispersed N-doped hierarchical porous carbon for trifunctional electrocatalyst. *Chem. Eng. J.* **2021**, *409*, 9.

(8) Wang, S. Y.; Guo, P.; Ma, G. S.; Wei, J.; Wang, Z. Y.; Cui, L.; Sun, L. L.; Wang, A. Y. Three-dimensional hierarchical mesoporous carbon for regenerative electrochemical dopamine sensor. *Electrochim. Acta* **2020**, *360*, No. 137016.

(9) Quintero-Jaime, A. F.; Quílez-Bermejo, J.; Cazorla-Amorós, D.; Morallón, E. Metal free electrochemical glucose biosensor based on N-doped porous carbon material. *Electrochim. Acta* **2021**, *367*, No. 137434.

(10) Zhang, C. M.; Zhang, R. Z.; Gao, X. H.; Cheng, C. F.; Hou, L.; Li, X. K.; Chen, W. Small Naked Pt Nanoparticles Confined in Mesoporous Shell of Hollow Carbon Spheres for High-Performance Nonenzymatic Sensing of H_2O_2 and Glucose. *ACS Omega* **2018**, *3*, 96−105.

(11) Yu, X. Q.; Zhang, Y. F.; Guo, L. P.; Wang, L. Macroporous carbon decorated with dendritic platinum nanoparticles: one-step synthesis and electrocatalytic properties. *Nanoscale* **2014**, *6*, 4806−4811.

(12) Zhang, X.; Zhang, L.; Zhu, G. G.; Zhu, Y. X.; Lu, S. Y. Mixed Metal Phosphide Chainmail Catalysts Confined in N-Doped Porous Carbon Nanoboxes as Highly Efficient Water-Oxidation Electrocatalysts with Ultralow Overpotentials and Tafel Slopes. *ACS Appl. Mater. Interfaces* **2020**, *12*, 7153−7161.

(13) Jia, H. X.; Shang, N. Z.; Feng, Y.; Ye, H. M.; Zhao, J. N.; Wang, H.; Wang, C.; Zhang, Y. F. Facile preparation of Ni nanoparticle embedded on mesoporous carbon nanorods for non-enzymatic glucose detection. *J. Colloid Interface Sci.* **2021**, *583*, 310−320.

(14) Dong, S. Y.; Zhang, D. D.; Cui, H.; Huang, T. L. ZnO/porous carbon composite from a mixed-ligand MOF for ultrasensitive electrochemical immunosensing of C-reactive protein. *Sens. Actuators, B* **2019**, *284*, 354−361.

(15) Hussain, M. Z.; Pawar, G. S.; Huang, Z.; Tahir, A. A.; Fischer, R. A.; Zhu, Y. Q.; Xia, Y. D. Porous ZnO/Carbon nanocomposites derived from metal organic frameworks for highly efficient photocatalytic applications: A correlational study. *Carbon* **2019**, *146*, 348−363.

(16) Hussain, M. Z.; Schneemann, A.; Fischer, R. A.; Zhu, Y.; Xia, Y. D. MOF Derived Porous ZnO/C Nanocomposites for Efficient Dye Photodegradation. *ACS Appl. Energy Mater.* **2018**, *1*, 4695−4707.

(17) Lewis, E. A.; Tolman, W. B. Reactivity of dioxygen-copper systems. *Chem. Rev.* **2004**, *104*, 1047−1076.

(18) Siwawut, J.; Namkhang, P.; Kongkachuichay, P. Co-Metal Catalysts on SiO_2-TiO_2 for Methanol Production from CO_2 - Effect of Preparation Methods. *Chem. Eng. Technol.* **2015**, *38*, 2153−2160.

(19) Li, D.; Liu, T. T.; Yan, Z. Y.; Zhen, L.; Liu, J.; Wu, J.; Feng, Y. J. MOF-Derived Cu_2O/Cu Nanospheres Anchored in Nitrogen-Doped Hollow Porous Carbon Framework for Increasing the Selectivity and Activity of Electrochemical CO_2-to-Formate Conversion. *ACS Appl. Mater. Interfaces* **2020**, *12*, 7030−7037.
(20) Gan, T.; Sun, J. Y.; Wu, Q.; Jing, Q. S.; Yu, S. Graphene Decorated with Nickel Nanoparticles as a Sensitive Substrate for Simultaneous Determination of Sunset Yellow and Tartrazine in Food Samples. *Electroanalysis* **2013**, *25*, 1505−1512.
(21) Sudha, V.; Senthil Kumar, S. M.; Thangamuthu, R. Hierarchical porous carbon derived from waste amla for the simultaneous electrochemical sensing of multiple biomolecules. *Colloids Surf., B* **2019**, *177*, 529−540.
(22) Wang, L. C.; Xie, L. N.; Feng, X.; Ma, H. H.; Li, X.; Zhou, J. B. Sustainable Lignin-Derived Hierarchical Porous Carbon for Supercapacitors: A Novel Approach for Holding Electrochemical Attraction Natural Texture Property of Precursor. *ACS Omega* **2021**, *6*, 33171−33179.
(23) Debbarma, J.; Mandal, P.; Saha, M. Fruit wastes to N-containing graphene: chemistry and mechanism. *Fullerenes, Nanotubes, Carbon Nanostruct.* **2021**, *29*, 739−745.
(24) Morelos-Gomez, A.; Mani-Gonzalez, P. G.; Aliev, A. E.; Munoz-Sandoval, E.; Herrera-Gomez, A.; Zakhidov, A. A.; Terrones, H.; Endo, M.; Terrones, M. Controlling the Optical, Electrical and Chemical Properties of Carbon Inverse Opal by Nitrogen Doping. *Adv. Funct. Mater.* **2014**, *24*, 2612−2619.
(25) Yang, X. P.; Xu, J.; Luo, N.; Tang, F. L.; Zhang, M. X.; Zhao, B. N,Cl co-doped fluorescent carbon dots as nanoprobe for detection of tartrazine in beverages. *Food Chem.* **2020**, *310*, 7.
(26) Liu, S.; Han, T. Y.; Wang, Z. Y.; Fei, T.; Zhang, T. Biomass-derived Nitrogen and Phosphorus Co-doped Hierarchical Micro/mesoporous Carbon Materials for High-performance Non-enzymatic H_2O_2 Sensing. *Electroanalysis* **2019**, *31*, 527−534.
(27) Zhao, Y.; Yang, L. J.; Chen, S.; Wang, X. Z.; Ma, Y. W.; Wu, Q.; Jiang, Y. F.; Qian, W. J.; Hu, Z. Can Boron and Nitrogen Co-doping Improve Oxygen Reduction Reaction Activity of Carbon Nanotubes? *J. Am. Chem. Soc.* **2013**, *135*, 1201−1204.
(28) Liu, Q.; Fan, J. C.; Min, Y. L.; Wu, T.; Lin, Y.; Xu, Q. J. B, N-codoped graphene nanoribbons supported Pd nanoparticles for ethanol electrooxidation enhancement. *J. Mater. Chem. A* **2016**, *4*, 4929−4933.
(29) Han, Q.; Sun, Y.; Shen, K. W.; Yan, Y.; Kang, X. J. Rapid determination of seven synthetic dyes in casual snacks based on packed-fibers solid-phase extraction coupled with HPLC-DAD. *Food Chem.* **2021**, *347*, No. 129026.
(30) Oymak, T.; Tokalioglu, S.; Cam, S.; Demir, S. Determination of color additive tartrazine (E 102) in food samples after dispersive solid phase extraction with a zirconium-based metal-organic framework (UiO-66(Zr)-$(COOH)_2$). *Food Addit. Contam., Part A* **2020**, *37*, 731−741.
(31) Feitosa, L. C. A.; Rodrigues, P. D.; Da Silva, A. S.; Rios, A. D.; Cladera-Olivera, F. Estimate of the theoretical maximum daily intake of Sunset Yellow FCF by the Brazilian population. *Food Addit. Contam., Part A* **2017**, *34*, 687−694.
(32) Vilian, A. T. E.; Kang, S. M.; Oh, S. Y.; Oh, C. W.; Umapathi, R.; Huh, Y. S.; Han, Y. K. A simple strategy for the synthesis of flower-like textures of Au-ZnO anchored carbon nanocomposite towards the high-performance electrochemical sensing of sunset yellow. *Food Chem.* **2020**, *323*, 9.
(33) Hajimahmoodi, M.; Afsharimanesh, M.; Moghaddam, G.; Sadeghi, N.; Oveisi, M. R.; Jannat, B.; Pirhadi, E.; Mazdeh, F. Z.; Kanan, H. Determination of eight synthetic dyes in foodstuffs by green liquid chromatography. *Food Addit. Contam., Part A* **2013**, *30*, 780−785.
(34) Huang, C. J.; Liu, Q. W.; Fan, W. J.; Qiu, X. Q. Boron nitride encapsulated copper nanoparticles: a facile one-step synthesis and their effect on thermal decomposition of ammonium perchlorate. *Sci. Rep.* **2015**, *5*, 16736.
(35) Yokoyama, Y.; Nanba, T.; Yasui, I.; Kaya, H.; Maeshima, T.; Isoda, T. X-ray Diffraction Study of the Structure of Silicon Nitride Fiber Made from Perhydropolysilazane. *J.Am. Ceram. Soc.* **1991**, *74*, 654−657.
(36) Guo, H. L.; Gao, Q. M. Boron and nitrogen co-doped porous carbon and its enhanced properties as supercapacitor. *J. Power Sources* **2009**, *186*, 551−556.
(37) Li, Y. J.; Gao, W.; Ci, L. J.; Wang, C. M.; Ajayan, P. M. Catalytic performance of Pt nanoparticles on reduced graphene oxide for methanol electro-oxidation. *Carbon* **2010**, *48*, 1124−1130.
(38) Ling, Z.; Wang, Z. Y.; Zhang, M. D.; Yu, C.; Wang, G.; Dong, Y. F.; Liu, S. H.; Wang, Y. W.; Qiu, J. S. Sustainable Synthesis and Assembly of Biomass-Derived B/N Co-Doped Carbon Nanosheets with Ultrahigh Aspect Ratio for High-Performance Supercapacitors. *Adv. Funct. Mater.* **2016**, *26*, 111−119.
(39) Chen, H.; Xiong, Y. C.; Yu, T.; Zhu, P. F.; Yan, X. Z.; Wang, Z.; Guan, S. Y. Boron and nitrogen co-doped porous carbon with a high concentration of boron and its superior capacitive behavior. *Carbon* **2017**, *113*, 266−273.
(40) Han, J. S.; Chung, D. Y.; Ha, D. G.; Kim, J. H.; Choi, K.; Sung, Y. E.; Kang, S. H. Nitrogen and boron co-doped hollow carbon catalyst for the oxygen reduction reaction. *Carbon* **2016**, *105*, 1−7.
(41) Ju, J.; Bai, J.; Bo, X. J.; Guo, L. P. Non-enzymatic acetylcholine sensor based on Ni-Al layered double hydroxides/ordered mesoporous carbon. *Electrochim. Acta* **2012**, *78*, 569−575.
(42) Sierra-Rosales, P.; Toledo-Neira, C.; Squella, J. A. Electrochemical determination of food colorants in soft drinks using MWCNT-modified GCEs. *Sens. Actuators, B* **2017**, *240*, 1257−1264.
(43) Gan, T.; Sun, J. Y.; Meng, W.; Song, L.; Zhang, Y. X. Electrochemical sensor based on graphene and mesoporous TiO_2 for the simultaneous determination of trace colourants in food. *Food Chem.* **2013**, *141*, 3731−3737.
(44) Yang, W. W.; Yu, Y. S.; Tang, Y.; Li, K. Y.; Zhao, Z.; Li, M. G.; Yin, G. P.; Li, H. B.; Sun, S. H. Enhancing electrochemical detection of dopamine via dumbbell-like FePt-Fe_3O_4 nanoparticles. *Nanoscale* **2017**, *9*, 1022−1027.
(45) Liu, M. X.; Gan, L. H.; Xiong, W.; Xu, Z. J.; Zhu, D. Z.; Chen, L. W. Development of MnO_2/porous carbon microspheres with a partially graphitic structure for high performance supercapacitor electrodes. *J. Mater. Chem. A* **2014**, *2*, 2555−2562.
(46) Guo, Z. Y.; Wang, F. M.; Xia, Y.; Li, J. L.; Tamirat, A. G.; Liu, Y. R.; Wang, L.; Wang, Y. G.; Xia, Y. Y. In situ encapsulation of core-shell-structured Co@Co_3O_4 into nitrogen-doped carbon polyhedra as a bifunctional catalyst for rechargeable Zn-air batteries. *J. Mater. Chem. A* **2018**, *6*, 1443−1453.
(47) Yu, L. L.; Mao, Y. X.; Gao, Y.; Qu, L. B. Sensitive and Simple Voltammetric Detection of Sudan I by Using Platinum Nanoparticle-Modified Glassy Carbon Electrode in Food Samples. *Food Anal. Methods* **2014**, *7*, 1179−1185.
(48) Rovina, K.; Acung, L. A.; Siddiquee, S.; Akanda, J. H.; Shaarani, S. M. Extraction and Analytical Methods for Determination of Sunset Yellow (E110)-A Review. *Food Anal. Methods* **2017**, *10*, 773−787.
(49) Diculescu, V. C.; Piedade, J. A. P.; Oliveira-Brett, A. M. Electrochemical behaviour of 2,8-dihydroxyadenine at a glassy carbon electrode. *Bioelectrochemistry* **2007**, *70*, 141−146.
(50) Wang, M. L.; Gao, Y. Q.; Sun, Q.; Zhao, J. W. Sensitively Simultaneous Determination of Sunset Yellow and Tartrazine in Foods Based on Polypyrrole Modified Oxidized Single-Walled Carbon Nanotubes. *J. Electrochem. Soc.* **2014**, *161*, B297−B304.
(51) Wang, M. L.; Zhao, J. W. Facile synthesis of Au supported on ionic liquid functionalized reduced graphene oxide for simultaneous determination of Sunset yellow and Tartrazine in drinks. *Sens. Actuators, B* **2015**, *216*, 578−585.
(52) Heli, H.; Hajjizadeh, M.; Jabbari, A.; Moosavi-Movahedi, A. A. Copper nanoparticles-modified carbon paste transducer as a biosensor for determination of acetylcholine. *Biosens. Bioelectron.* **2009**, *24*, 2328−2333.

https://doi.org/10.1021/acsomega.2c03319
ACS Omega 2022, 7, 32068−32077

(53) Wu, X.; Zhang, X. J.; Zhao, C. J.; Qian, X. Z. One-pot hydrothermal synthesis of ZnO/RGO/ZnO@Zn sensor for sunset yellow in soft drinks. *Talanta* **2018**, *179*, 836−844.
(54) Deng, K. Q.; Li, C. X.; Li, X. F.; Huang, H. W. Simultaneous detection of sunset yellow and tartrazine using the nanohybrid of gold nanorods decorated graphene oxide. *J. Electroanal. Chem.* **2016**, *780*, 296−302.
(55) Qiu, X. L.; Lu, L. M.; Leng, J.; Yu, Y. F.; Wang, W. M.; Jiang, M.; Bai, L. An enhanced electrochemical platform based on graphene oxide and multi-walled carbon nanotubes nanocomposite for sensitive determination of Sunset Yellow and Tartrazine. *Food Chem.* **2016**, *190*, 889−895.
(56) Rouhani, S. Novel Electrochemical Sensor for Sunset Yellow Based on a Platinum Wire-Coated Electrode. *Anal. Lett.* **2009**, *42*, 141−153.
(57) Ghoreishi, S. M.; Behpour, M.; Golestaneh, M. Simultaneous determination of Sunset yellow and Tartrazine in soft drinks using gold nanoparticles carbon paste electrode. *Food Chem.* **2012**, *132*, 637−641.
(58) He, Q. G.; Liu, J.; Liu, X. P.; Xia, Y. H.; Li, G. L.; Deng, P. H.; Chen, D. C. Novel Electrochemical Sensors Based on Cuprous Oxide-Electrochemically Reduced Graphene Oxide Nanocomposites Modified Electrode toward Sensitive Detection of Sunset Yellow. *Molecules* **2018**, *23*, 2130.

https://doi.org/10.1021/acsomega.2c03319
ACS Omega 2022, 7, 32068−32077